Chromospheric Heating from Local Magnetic Growth and Ambipolar Diffusion under Nonequilibrium Conditions

Juan Martínez-Sykora[1,2,3,4] , Jaime de la Cruz Rodríguez[5] , Milan Gošić[1,2] , Alberto Sainz Dalda[1,2] ,
Viggo H. Hansteen[1,2,3,4] , and Bart De Pontieu[1,3,4]

[1] Lockheed Martin Solar & Astrophysics Laboratory, 3251 Hanover Street, Palo Alto, CA 94304, USA; martinezsykora@baeri.org
[2] Bay Area Environmental Research Institute, NASA Research Park, Moffett Field, CA 94035, USA
[3] Rosseland Centre for Solar Physics, University of Oslo, P.O. Box 1029 Blindern, NO-0315 Oslo, Norway
[4] Institute of Theoretical Astrophysics, University of Oslo, P.O. Box 1029 Blindern, NO-0315 Oslo, Norway
[5] Institute for Solar Physics, Dept. of Astronomy, Stockholm University, AlbaNova University Centre, SE-10691 Stockholm, Sweden

Abstract

The heating of the chromosphere in internetwork regions remains one of the foremost open questions in solar physics. In the present study, we tackle this old problem by using a very-high-spatial-resolution simulation of quiet-Sun conditions performed with radiative MHD numerical models and interface region imaging spectrograph (IRIS) observations. We have expanded a previously existing 3D radiative MHD numerical model of the solar atmosphere, which included self-consistently locally driven magnetic amplification in the chromosphere, by adding ambipolar diffusion and time-dependent nonequilibrium hydrogen ionization to the model. The energy of the magnetic field is dissipated in the upper chromosphere, providing a large temperature increase due to ambipolar diffusion and nonequilibrium ionization (NEQI). At the same time, we find that adding the ambipolar diffusion and NEQI in the simulation has a minor impact on the local growth of the magnetic field in the lower chromosphere and its dynamics. Our comparison between synthesized Mg II profiles from these high-spatial-resolution models, with and without ambipolar diffusion and NEQI, and quiet-Sun and coronal hole observations from IRIS now reveal a slightly better correspondence. The intensity of profiles is increased, and the line cores are slightly broader when ambipolar diffusion and NEQI effects are included. Therefore, the Mg II profiles are closer to those observed than in previous models, though some differences still remain.

Unified Astronomy Thesaurus concepts: Quiet solar chromosphere (1986); Radiative magnetohydrodynamics (2009); Solar photosphere (1518); Solar magnetic fields (1503); Magnetohydrodynamical simulations (1966); Magnetohydrodynamics (1964)

1. Introduction

In the chromosphere, a complex force balance originating from gas pressure gradients and magnetic forces gives rise to a highly dynamic and complex atmospheric structure given the ubiquitous presence of nonlinear waves (e.g., Carlsson & Stein 1994, 2002) and small-scale magnetic fields (e.g., Lites et al. 2008). However, comparisons between radiative (M)HD models and high-resolution observations showed insufficient wave power in the upper chromosphere (e.g., Carlsson et al. 2007), although this remains a topic of discussion (Molnar 2022). On the other hand, the weak magnetic fields that continuously emerge on granular scales and that are thought to be generated by a local dynamo have also been detected in numerical models (Abbett 2007), and they have enormous potential for heating the low solar atmosphere. Recently, Amari et al. (2015) used models to suggest that the local dynamo in the upper convection zone could maintain the heating of the whole solar atmosphere. However, radiative MHD models indicate that the strong entropy drop at the solar surface leads to a net negative Poynting flux and strong superadiabaticity, making it very difficult for the magnetic field to reach the chromosphere (e.g., Abbett 2007; Nordlund 2008; Moreno-Insertis et al. 2018). Similarly, there has been limited

observational evidence for tracking internetwork (IN) emerging fields from the photosphere into the chromosphere and above, and the production of localized heating (e.g., Martínez González & Bellot Rubio 2009; Gošić et al. 2016, 2021).

In addition to waves and shocks, another potential mechanism to transfer energy to greater heights are swirls (e.g., Yadav et al. 2020). However, in principle, this mechanism does not lead to the transport of the magnetic flux, but kinetic energy and its role in heating the chromosphere is unclear. As an alternative scenario, Martínez-Sykora et al. (2019) showed that the magnetoacoustic shocks in the chromospheric IN regions in the quiet Sun (QS) or coronal hole (CH) could convert kinetic energy into magnetic energy, i.e., producing a local magnetic energy growth in the chromosphere. That study lacked a proper model of ambipolar diffusion (also known as Pedersen resistivity) and nonequilibrium ionization (NEQI) for hydrogen. The former represents an efficient mechanism to dissipate currents (Khomenko & Collados 2012; Martínez-Sykora et al. 2017; Khomenko et al. 2018), whereas the latter has a profound effect on the temperature, ionization fraction, and electron densities in the chromosphere (Leenaarts et al. 2007; Golding et al. 2016). Knowing the ionization fraction accurately is necessary in order to calculate the ambipolar diffusivity, and therefore including NEQI of hydrogen is required in order to also model precisely the heating caused by ambipolar diffusion (Khomenko et al. 2014; Martínez-Sykora et al. 2020; Nóbrega-Siverio et al. 2020). In the current work, we expand the model presented in Martínez-Sykora et al. (2019) by including

ambipolar diffusion, and the hydrogen ionization is treated under NEQI conditions, allowing us to investigate its role in chromospheric heating.

2. Numerical Models

Our 3D radiative MHD numerical simulation is computed with the Bifrost code (Gudiksen et al. 2011). The model includes radiative transfer with scattering in the photosphere and lower chromosphere (Skartlien 2000; Hayek et al. 2010). In the middle and upper chromosphere, radiation from specific species such as hydrogen, calcium, and magnesium is computed following Carlsson & Leenaarts (2012) recipes while using optically thin radiative losses in the transition region and corona. Thermal conduction along the magnetic field is important for the energetics of the transition region and corona. The main difference with the model presented in Martínez-Sykora et al. (2019) is that the current simulation treats the hydrogen ionization in nonequilibrium conditions (Leenaarts et al. 2007) and the ion-neutral interaction effects by including the ambipolar diffusion (Martínez-Sykora et al. 2020; Nóbrega-Siverio et al. 2020).

The simulation spans in the vertical axis a range of heights from ∼2.5 Mm below the photosphere to 8 Mm above into the corona with a nonuniform vertical grid size, with the smallest grid size of 4 km in the photosphere and chromosphere. The photosphere is located at $z = 0$, where optical depth at 500 nm is $\tau_{500} \sim 1$. The horizontal domain spans 6×6 Mm in the x- and y-directions with 5 km resolution. Initially, the simulation box is seeded with a uniform weak vertical magnetic field of 2.5 G. The convective motion builds magnetic field complexity, and as a result, the magnetic field strength reaches a statistical steady state with $B_{rms} = 57$ G, average $|B_z| = 17$ G with some flux concentrations reaching 2 kG at photospheric heights (similar to that described by Vögler & Schüssler 2007; Rempel 2014; Cameron & Schüssler 2015).

In this high-resolution QS model, the chromospheric magnetic energy content increases substantially with time, especially in the region that is dominated by shock waves and where plasma $\beta > 1$ $(0.5 < z < 2$ Mm). Essentially, the magnetic energy is growing in place while it is being fed by the dynamics of the model. The magnetic growth is produced by colliding shocks and shear flows instead of the turbulent motion of the convective cells in the convection zone. Further details of this model can be found in Martínez-Sykora et al. (2019). After the magnetic field has reached a statistically steady state, some ∼25 minutes into the run, ambipolar diffusion and NEQI are turned on. The simulation is then run for another ∼10 minutes, which allows the transition from local thermodynamic equilibrium (LTE) to an NEQI and ambipolar diffusion to settle.

3. Spectral Synthesis

We have computed the Mg II h and k synthetic profiles using the 1.5D parallel version of the Rybicki & Humme (1991) radiative transfer code (Uitenbroek 2001; Pereira & Uitenbroek 2015). The model atom consists of 10 bound levels plus the Mg III continuum (Leenaarts et al. 2013). Partial redistribution of the frequency in the scattered radiation has been included in the modeling of the Mg II h and k lines by using the fast angle approximation proposed by Leenaarts et al. (2012). The radiative transfer equation was solved using cubic

Bezier splines solvers (de la Cruz Rodríguez & Piskunov 2013).

4. Observations

In this article, we used the already analyzed interface region imaging spectrograph (IRIS) (De Pontieu et al. 2014) data set presented in Martínez-Sykora et al. (2022). The observations were obtained on 2016 March 25 and 2017 October 15. The observations include an equatorial CH, starting at 10:09:18 UT and ending 11:58:45 UT, and a QS region from 17:54:22 UT until 22:52:35 UT. Both observations were taken at the disk center. We separate the IN field from the network field (NE) and refer to Martínez-Sykora et al. (2022) for further details.

5. Results

In both simulations, i.e., without and with ambipolar diffusion and NEQI, the vertical magnetic field slice (panels (c) and (f) in Figure 1) reveals the highly complex salt and pepper mixture in the low and middle chromosphere ($z \sim [0.5, 2]$ Mm) induced by the kinematics as described in detail by Martínez-Sykora et al. (2019) and Martínez-Sykora et al. (2022). This magnetic energy is created in situ due to the shocks (panel (b)) traveling through, which fold, stretch, twist, and reconnect the magnetic field, thereby building up its energy.

The kinetic energy per particle does not change significantly with time as the ambipolar diffusion and NEQI effects are turned (top panel of Figure 2). The instance shown in the figure for the generalized Ohm's law and nonequilibrium ionization (GOL&NEQ) case is 10 minutes after NEQI and ambipolar diffusion has turned on. We see only a small shift to greater heights (by ∼100 km) of the kinetic energy per particle profile with height.

Interestingly, the ambipolar diffusion (and ambipolar heating, panel (h) in Figure 1) is taking place just at the top (upper chromosphere, $z \sim [1.5, 3.5]$ Mm) of the location of the in situ chromospheric magnetic growth (lower and mid chromosphere, $z \sim [0.5, 2]$ Mm). Consequently, the ambipolar diffusion is not "annihilating" the local magnetic growth due to the conversion from kinetic to magnetic energy. This can be appreciated in the time evolution of the magnetic field strength and kinetic energy per particle rms and the averaged absolute vertical magnetic field as a function of height once the NEQI and ion-neutral interaction effects have been turned on. The middle panel of Figure 2 shows that the magnetic field is maintained in time in the low and mid chromosphere and dissipated in time at greater heights. While the magnetic field rms provides a perhaps more intuitive representation of the magnetic energy (middle panel), the averaged absolute vertical magnetic field (bottom panel) allows us to visualize where the diffusion is more significant and the role of Poynting flux. From the bottom panel, it is clear that diffusion is above 1 Mm, and there is no apparent transport of the magnetic field in time.

The ambipolar diffusion is inversely proportional to the ionization fraction, and panel (i) suggests that the ambipolar diffusion should be higher in deeper layers. However, it is also inversely proportional to the ion-neutral collision frequency. This decreases drastically with height as the density drops (not shown here; see also Wargnier et al. 2022).

The ambipolar diffusion dissipates substantial magnetic energy introduced into the mid and upper chromosphere from
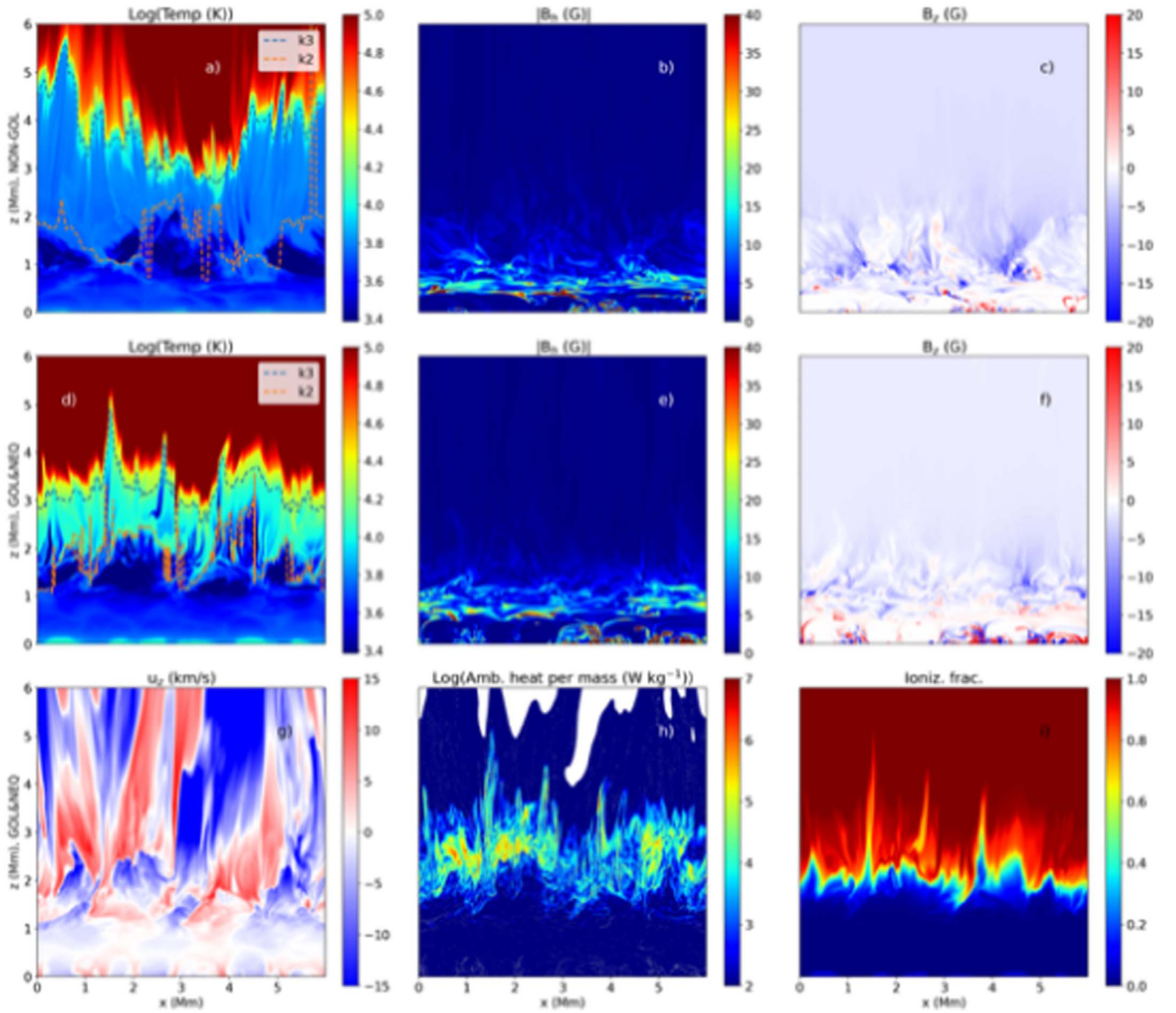
Figure 1. Top row shows the simulation without NEQI and ambipolar diffusion (non-GOL) and second and third row includes NEQI and ambipolar diffusion (GOL&NEQ) 10 minutes after adding the new physical processes. Panels (a)–(c) and (d)–(f) show vertical cut maps of temperature, horizontal field strength, and vertical field strength, respectively. For GOL&NEQ, panels (g) to (i) show vertical velocity, ambipolar heating, and ionization fraction. The height for optical depth (τ) equal to unity at the Mg II k_2 and k_3 locations has been added in panels (a) and (d). In the convection zone ($z < 0$), the magnetic field is accumulated in the downflows. Shocks dominate the simulated chromosphere ($0.8 < z < 2$ Mm) and jets ($2 < z < 4$ Mm), whereas the corona is maintained by energy released from magnetic braiding and dominated by thermal conduction.

in situ chromospheric magnetic growth. Consequently, the magnetic energy in the upper chromosphere and above decreases with time (bottom panel of Figure 2). The magnetic energy in the upper chromosphere arises from the complex evolution of the magnetic field due to waves, currents, and colliding shocks traveling through the atmosphere. It is these currents that are dissipated by ambipolar diffusion.

The effects of dissipation of these currents have a significant effect on the thermodynamics of the upper chromosphere. These effects are substantially modified by NEQI effects. Compared to LTE ionization, the spatial maps of ionization degree in NEQI show a less sharp transition from partial ionization to full ionization (panel (i) in Figure 1). In addition, it is known that recombination takes longer, so the plasma

remains ionized for longer (Leenaarts et al. 2007; Martínez-Sykora et al. 2020). The latter two papers showed that under NEQI conditions, dissipation of energy causes a temperature increase for a short time (of order several seconds, depending on the local conditions) before ionization occurs instead of immediately ionizing the plasma. Note that the amount of neutrals in the mid-upper chromosphere is relatively low. Therefore, although the ionization may take a few seconds, most of the heating from the dissipation of currents (through ambipolar diffusion) increases the plasma temperature. As a result, the temperature rises by several thousands of kelvins, which produces an upper chromosphere of $\sim 10^4$ K, as seen by comparing panels (a) and (d) from Figure 1. Note that the location of the strongest magnetic field values or of the
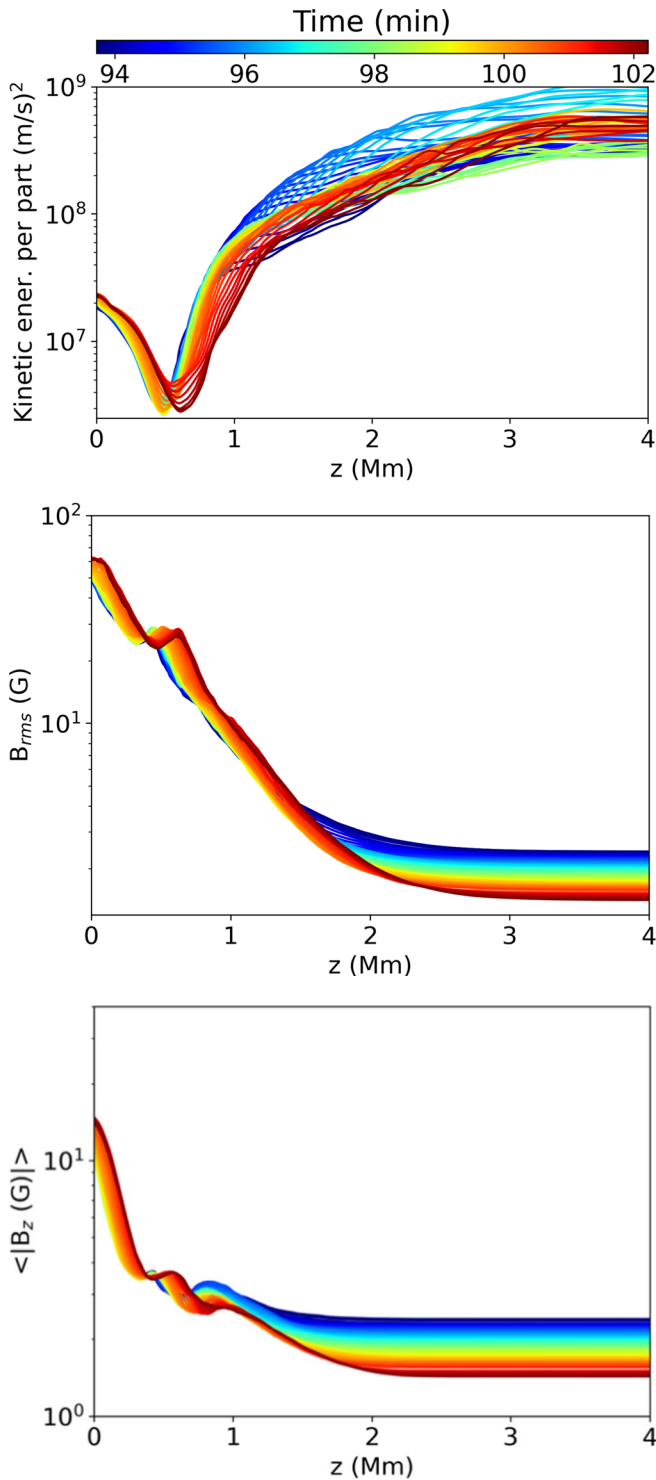
Figure 2. Kinetic energy (top) per particle rms, magnetic field strength (middle), and the average of the absolute vertical magnetic field (bottom) as a function of height (horizontal axis) and time (color bar) reveals that the ambipolar diffusion and NEQI effects do not change substantially the magnetic field growth of kinetic energy. The time range in this plot shows the evolution after both effects have been turned on. The ambipolar diffusion dissipates magnetic energy in the upper chromosphere.

velocities in the chromosphere ($z = [0.5, 1.5]$ Mm) has, statistically speaking, barely changed at that instance (compare panels (b) and (c) with (e) and (f)).

We have computed the radiative transfer for Mg II chromospheric lines for these two instances shown in Figure 1.

However, before we compare the synthesis of these two models and with IRIS observations, we point out that $\tau = 1$ within the wavelength range of k_2 and k_3 is within the upper chromosphere in both models (contours in panel (a) and (d) of Figure 1). Consequently, the line core captures the region that has been heated due to local magnetic growth and ambipolar diffusion.

We compare synthetic Mg II k line from on-disk QS and CH targets separating IN and NE fields. Due to the highly simplified and weak initial magnetic field and dimensions of the numerical domain, the model is closer to mimicking an IN region in a CH or QS than an NE field. The synthesis before (red) and after (blue) of the ambipolar diffusion and NEQI are turned on are compared with the observations (Figure 3). In addition, we consider IRIS spectral broadening by convolving the synthetic profiles with a Gaussian with an FWHM of 0.056 Å (dashed lines, Pereira et al. 2013).

We find that the synthetic profiles (solid lines) are asymmetric with a very strong blue peak. This asymmetry comes from the fact that k_3 is redshifted, which can be caused by a nonzero net downflow in the upper chromosphere. A more complex field topology with NE surrounding the IN field may produce a balanced net flow in the upper chromosphere and center the Mg II h_3/k_3 wavelength location more.

The convolution also broadens the profiles slightly and reduces the peak intensity. The NEQI and ambipolar effects lead to profiles with stronger intensities, and the profiles are also somewhat broader than those without those effects. Carlsson et al. (2015) showed that a hotter and denser upper chromosphere can broaden Mg II profiles. Nevertheless, despite the combination of including effects from ambipolar diffusion, local magnetic growth, and NEQI effects that result in a hotter chromosphere, and the IRIS instrumental broadening, the spectral profiles remain slightly narrower than in the observations. This suggests that this model may be missing more physical processes or includes a too simplified magnetic field topology; see the discussion for further details.

6. Discussion

Martínez-Sykora et al. (2019) presented a new possible mechanism for amplifying chromospheric magnetic field by converting the kinetic energy into magnetic energy in situ in the QS or CH IN regions. In this work, we have extended this model by now adding NEQI of hydrogen and ambipolar diffusion. We found that the magnetic energy growth in the chromosphere continues to occur in the presence of these two physical processes. The ambipolar diffusion becomes important just above the layer where magnetic field growth occurs in the chromosphere. Ambipolar diffusion helps to convert magnetic energy into thermal energy in the upper chromosphere. The NEQI effects ensure that the ionization fraction is such that the ambipolar diffusion dissipates magnetic energy in the upper chromosphere and that this dissipation increases temperature instead of ionizing the plasma. As a result, the upper chromosphere reaches temperatures above $\sim 10^4$ K. Note that NEQI effects are crucial to accurately estimate the ambipolar diffusion since the ambipolar diffusivity is proportional to the ionization degree (see also Martínez-Sykora et al. 2020; Nóbrega-Siverio et al. 2020, for different topologies).

The hotter upper chromosphere that we find in the new model has an effect on the spectral diagnostics that are formed in this region. We have compared the IRIS Mg II profiles
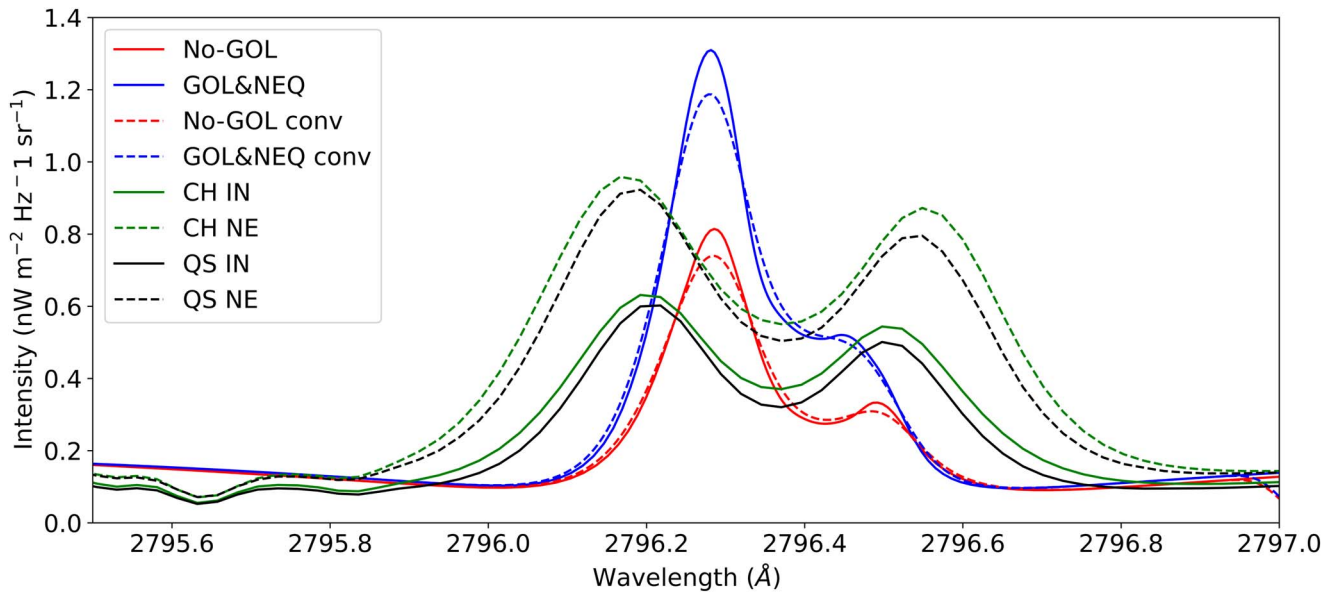
Figure 3. The synthesis of Mg II k before (red) and after (blue) the ambipolar diffusion and NEQI has been turned on are compared with QS (black) and CH (green) IRIS observations. The observations have been separated into IN (solid) and NE (dashed) field regions, as detailed in Martínez-Sykora et al. (2022). In addition, the synthetic profiles have been convolved with IRIS instrumental spectral broadening (∼0.056 Å FWHM, dashed lines).

observations of CH and QS regions and separated between locations of IN and NE fields, similar to what was done in Martínez-Sykora et al. (2022). The results shown here have been done for Mg II k, but we note that the conclusions also apply to Mg II h (not shown here) since the h and k lines show the same behavior. Our models' synthetic Mg II peaks are too asymmetric, with stronger intensities in the red peak (k2v) compared to the observations. We note that the field configuration in our simulation is highly simplified without any NE field surrounding the IN field and a relatively weak coronal magnetic field. This simplified field topology may contribute to having larger net flows in the upper chromosphere and skew the Mg II profiles.

In addition, we have found that the profiles increase in intensity and slightly broaden due to a temperature increase in the upper chromosphere when the NEQI effects and ambipolar diffusion are considered. We find that observations show somewhat broader profiles than the synthetic observables (in Hansteen et al. 2022, one can appreciate the improvement on the synthetic profiles of the simulations presented in this work with other simulations with lower-resolution models and somewhat different field configurations). Therefore, the radiative MHD model or the radiative transfer treatment for the synthesis may be missing some physical processes. On the one hand, the radiative transfer calculations are based on the 1.5D approximation ignoring 3D radiative transfer effects, which may play a role in the core of the Mg II line (Judge et al. 2020). It is unclear, however, how these 3D effects would lead to broader profiles. On the other hand, the narrower Mg II core profile in the simulations could come from a lack of complexity in the line of sight (LOS) velocity field, turbulence, mass loading into the upper chromosphere, and/or a lack of heating. Extending the upper-chromospheric conditions to deeper layers can also broaden the Mg II profiles. In our simulation, we assumed that the plasma could be treated as a single fluid. It is possible that microphysics or other multifluid effects may lead to significant changes in turbulence, heating, and spatial extent of the region with upper-chromospheric conditions, and thus to broader Mg II profiles. For instance, Oppenheim et al. (2020) and Evans et al. (2022) suggest

that the colder regions of the simulated atmosphere are where the thermal Farley–Buneman instability (Dimant et al. 2022) will grow and, hence, the large-scale single fluid assumptions fail in those locations. Indeed, it is found that the Farley–Buneman and thermal instabilities could lead to microturbulence and heating (Oppenheim et al. 2020; Evans et al. 2022).

ORCID iDs

Juan Martínez-Sykora ● https://orcid.org/0000-0002-0333-5717
Jaime de la Cruz Rodríguez ● https://orcid.org/0000-0002-4640-5658

Milan Gošić ● https://orcid.org/0000-0002-5879-4371
Alberto Sainz Dalda ● https://orcid.org/0000-0002-3234-3070
Viggo H. Hansteen ● https://orcid.org/0000-0003-0975-6659
Bart De Pontieu ● https://orcid.org/0000-0002-8370-952X

References

Abbett, W. P. 2007, ApJ, 665, 1469
Amari, T., Luciani, J.-F., & Aly, J.-J. 2015, Natur, 522, 188
Cameron, R., & Schussler, M. 2015, Sci, 347, 1333
Carlsson, M., Hansteen, V. H., de Pontieu, B., et al. 2007, PASJ, 59, 663
Carlsson, M., & Leenaarts, J. 2012, A&A, 539, A39
Carlsson, M., Leenaarts, J., & Pontieu, B. D. 2015, ApJL, 809, L30
Carlsson, M., & Stein, R. F. 1994, in Chromospheric Dynamics, ed. M. Carlsson (Oslo: University of Oslo), 47
Carlsson, M., & Stein, R. F. 2002, ApJ, 572, 626
de la Cruz Rodríguez, J., & Piskunov, N. 2013, ApJ, 764, 33
De Pontieu, B., Title, A. M., Lemen, J. R., et al. 2014, SoPh, 289, 2733
Dimant, Y. S., Oppenheim, M. M., Evans, S., & Martinez-Sykora, J. 2022, arXiv:2211.05264
Evans, S., Oppenheim, M., Martínez-Sykora, J., Dimant, Y., & Xiao, R. 2022, arXiv:2211.03644
Golding, T. P., Leenaarts, J., & Carlsson, M. 2016, ApJ, 817, 125
Gošić, M., Pontieu, B. D., Bellot Rubio, L. R., Sainz Dalda, A., & Pozuelo, S. E. 2021, ApJ, 911, 41
Gošić, M., Rubio, L. R. B., Iniesta, J. C. d. T., Suarez, D. O., & Katsukawa, Y. 2016, ApJ, 820, 35
Gudiksen, B. V., Carlsson, M., Hansteen, V. H., et al. 2011, A&A, 531, A154
Hansteen, V., Martinez Sykora, J., Carlsson, M., et al. 2022, arXiv:2211.09277
Hayek, W., Asplund, M., Carlsson, M., et al. 2010, A&A, 517, A49
Judge, P. G., Kleint, L., Leenaarts, J., Sukhorukov, A. V., & Vial, J.-C. 2020, ApJ, 901, 32
Khomenko, E., & Collados, M. 2012, ApJ, 747, 87
Khomenko, E., Collados, M., Díaz, A., & Vitas, N. 2014, PhPl, 21, 092901
Khomenko, E., Vitas, N., Collados, M., & de Vicente, A. 2018, A&A, 618, A87
Leenaarts, J., Carlsson, M., Hansteen, V., & Rutten, R. J. 2007, A&A, 473, 625
Leenaarts, J., Pereira, T., & Uitenbroek, H. 2012, A&A, 543, A109
Leenaarts, J., Pereira, T. M. D., Carlsson, M., Uitenbroek, H., & De Pontieu, B. 2013, ApJ, 772, 89
Lites, B. W., Kubo, M., Socas-Navarro, H., et al. 2008, ApJ, 672, 1237
Martinez Gonzalez, M. J., & Bellot Rubio, L. R. 2009, ApJ, 700, 1391
Martínez-Sykora, J., Hansteen, V. H., Gudiksen, B., et al. 2019, ApJ, 878, 40
Martínez-Sykora, J., Leenaarts, J., De Pontieu, B., et al. 2020, ApJ, 889, 95
Martínez-Sykora, J., Pontieu, B. D., Carlsson, M., et al. 2017, ApJ, 847, 36
Martínez-Sykora, J., Sainz Dalda, A., Gosic, M., & De Pontieu, B. 2022, arXiv:2210.15150
Molnar, M. E. 2022, PhD thesis, Astrophysical and Planetary Sciences, University of Colorado at Boulder
Moreno-Insertis, F., Martínez-Sykora, J., Hansteen, V. H., & Munoz, D. 2018, ApJL, 859, L26
Nóbrega-Siverio, D., Moreno-Insertis, F., Martínez-Sykora, J., Carlsson, M., & Szydlarski, M. 2020, A&A, 633, A66
Nordlund, Å. 2008, PhST, 133, 014002
Oppenheim, M., Dimant, Y., Longley, W., & Fletcher, A. C. 2020, ApJL, 891, L9
Pereira, T. M. D., Leenaarts, J., De Pontieu, B., Carlsson, M., & Uitenbroek, H. 2013, ApJ, 778, 143
Pereira, T. M. D., & Uitenbroek, H. 2015, A&A, 574, A3
Rempel, M. 2014, ApJ, 789, 132
Rybicki, G. B., & Hummer, D. G. 1991, A&A, 245, 171
Skartlien, R. 2000, ApJ, 536, 465
Uitenbroek, H. 2001, ApJ, 557, 389
Vögler, A., & Schüssler, M. 2007, A&A, 465, L43
Wargnier, Q. M., Martínez-Sykora, J., Hansteen, V. H., & De Pontieu, B. 2022, ApJ, 933, 205
Yadav, N., Cameron, R. H., & Solanki, S. K. 2020, ApJL, 894, L17